ACS OMEGA

http://pubs.acs.org/journal/acsodf

Article

High-Efficiency Photocatalytic Degradation of Tannic Acid Using TiO_2 Heterojunction Catalysts

Ruixi Liu, Linzhen Wu, Hao Liu, Youkui Zhang, Jianjun Ma, Cairong Jiang,* and Tao Duan*

Cite This: *ACS Omega* 2021, 6, 28538−28547

Read Online

ACCESS | Metrics & More | Article Recommendations | Supporting Information

ABSTRACT: Photocatalysts have been extensively used for hydrogen evolution or organic degradation. In this work, two different heterojunction types of composite photocatalysts, 1T-MoS_2@TiO_2 with Schottky heterojunction and 2H-MoS_2@TiO_2 with type-II heterojunction, are synthesized via hydrothermal synthesis. These two composite materials exhibit excellent photocatalytic activity toward the degradation of tannic acid, which is a typical organic in nuclear wastewater. At an optimal loading of 16% 1T-MoS_2, the 1T-MoS_2@TiO_2 shows the highest degradation capacity of 98%, which is 3.2 times higher than that of pure TiO_2. The degradation rate of 16% 1T-MoS_2@TiO_2 is much higher than that of 13% 2H-MoS_2@TiO_2. The enhanced photocatalytic activity might be attributed to the improved charge transfer according to the mechanism investigation, supported by the X-ray photoelectron spectroscopy (XPS) and electrochemical impedance spectroscopy (EIS) analyses. This work provides new opportunities for constructing highly efficient catalysts for nuclear waste disposal.

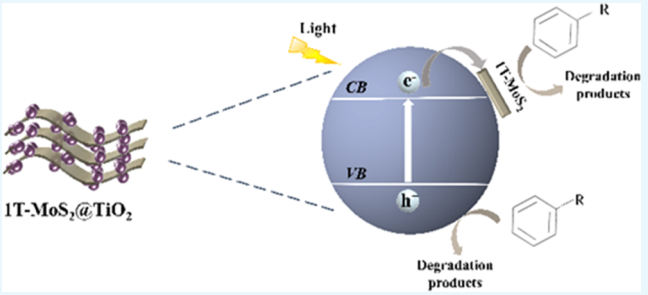

1. INTRODUCTION

Nuclear energy is a nonrenewable alternative energy source with high energy density, environmental protection, and a small footprint.[1−3] However, radioactive organic wastewater is produced in nuclear fuel production, operation of nuclear power plants, and decommissioning of nuclear facilities, which causes long-term harm to the ecological environment. Organic nuclear waste liquid mainly consists of the radioactive element uranium, organic matter tannic acid (TA), and tributyl phosphate. It has the characteristics of complex composition, intense radioactivity, poor safety and stability, and a high amount of heat generation.[4] The presence of organic matter not only easily causes the blockage and regeneration of the ion exchange resin channel but also has potential safety hazards. Therefore, it is required to pretreat the organic matter before solidifying the radioactive waste liquid containing organic matter.

Traditional methods for removing organic matter include high-temperature oxidation, wet chemical reaction, physical adsorption, photocatalysis, etc. Among them, the semiconductor photocatalysis technology displays many advantages, for example, strong oxidizing ability, effective absorption of light, environment friendliness, mild reaction conditions, and stable chemical properties without secondary pollutants. It has become a research focus in energy and the environment.[5,6] The photocatalytic efficiency depends on the light absorption intensity and carrier transfer efficiency of photocatalysts. To date, excellent materials such as graphene,[7−12] molybdenum disulfide,[13−19] and titanium dioxide (TiO_2) have been developed for the photocatalytic processes.[20−29]

Anatase TiO_2 material used as a photocatalyst demonstrates high efficiency and excellent chemical stability. The main characteristics of anatase TiO_2 are its nontoxicity, low cost, and strong corrosion resistance. Therefore, it is widely used in the photocatalytic field.[20,30−35] Solar energy, generated through photoelectricity and water photocatalysis over photocatalysts (e.g. TiO_2), can alleviate the environmental and energy crisis.[36−38] TiO_2 wide band gap, high electron−hole recombination rate, and few active catalytic sites are the main obstacles hindering its wide application.[39,40] It is therefore interesting to develop new photocatalytic materials with good photocatalytic activities or tailor the structure and particle size. It is found that nanoflower TiO_2 has better degradation ability toward methylene blue than pure TiO_2.[41]

Developing heterojunction materials is another effective method to accelerate charge separation, activate the catalyst surface, and enhance photocatalytic active sites.[42] New composite materials synthesized with metals or semiconductors contain the Schottky barrier heterojunctions. Therefore,

Received: May 12, 2021
Accepted: July 8, 2021
Published: October 22, 2021

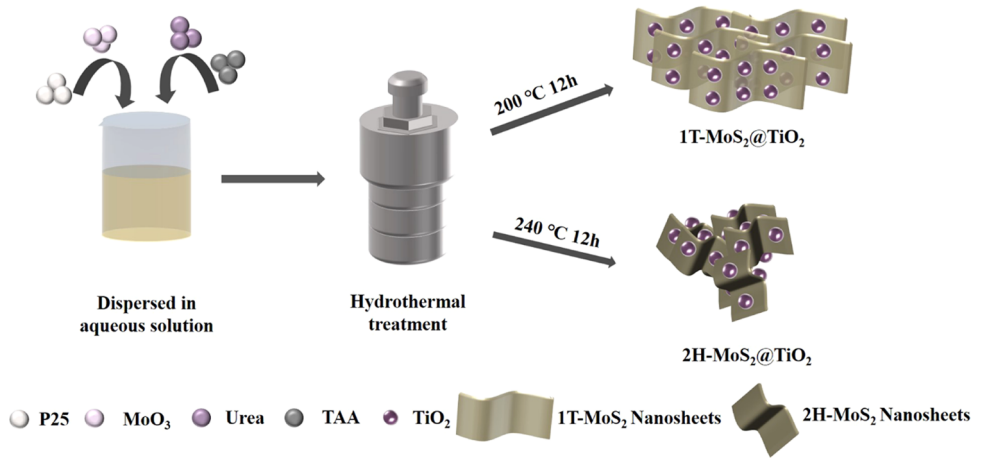

Figure 1. Schematic diagram of the procedure of preparing a composite material (1T/2H) MoS_2@TiO_2.

they are often used for photocatalytic hydrogen evolution.[43] However, some metals are high-cost, and hence it is necessary to seek alternatives. The CdSe/graphene/TiO_2 composite prepared shows high photocatalytic activity for methylene blue under visible light.[7] type-II heterojunctions have been proven to be promising excellent photocatalytic materials.[44,45] The large exposed edge of MoS_2 originates from the rich catalytic active sites on the sulfur edge of the crystal layer, and the narrow band gap has good complementary characteristics with TiO_2.[26,46−49] Yuan et al. loaded MoS_2 on TiO_2 to construct a type-II heterostructure material for efficient solar hydrogen production.[50] Tang et al. synthesized a series of anatase TiO_2@MIL-101(Cr) by the solvothermal method for photocatalytic degradation of bisphenol A (BPA) and 59% TiO_2@MIL-101(Cr) could achieve 99.4% degradation rate within 240 min under ultraviolet light irradiation.[51] Therefore, MoS_2@TiO_2 heterojunction materials have the advantages of large specific surface area, excellent electron transfer ability, and enhanced active sites in theory. However, there is still less information for applying these kinds of composite materials in the degradation of pollutants in nuclear wastewater.

Tannic acid is one of the important components of organic acids in nuclear waste liquid, and it is prone to the complex reaction of metals. If tannic acid is discharged into water, it will cause serious pollution of the water body, reduce the content of organic matter in the water, and be toxic to organisms in the water. Therefore, green and safe degradation of tannic acid has important practical significance. A 98% tannic acid was successfully degraded by titanium oxide-coated magnetic activated carbon under ultraviolet light for 150 min with improved stability.[52] Qiu et al.[53] prepared nano-TiO_2-coated tiles for photocatalytic degradation experiments. The photocatalytic device was selected as a UV lamp; the results showed that the degradation rate after 6 h reached 76% and Fe−N codoped SiO_2@TiO_2 could degrade 99% of tannic acid in 80 min.[54]

In this work, two new composites, 1T-MoS_2@TiO_2 with a rich 1T-MoS_2 heterojunction and 2H-MoS_2@TiO_2 with type-II heterojunction, were synthesized.[55] The photocatalytic performance of using these two types of materials for the photocatalytic degradation of tannic acid in nuclear wastewater have been investigated. The effect of the compositions of MoS_2 on the photocatalytic activity has been studied and the optimized MoS_2 content has been evaluated.

2. EXPERIMENTAL SECTION

2.1. Materials. Raw chemicals, molybdenum trioxide (MoO_3, 99.9% Shanghai Aladdin Biochemical Technology Co., Ltd.), urea (CH_4N_2O, 99%, Shanghai Aladdin Biochemical Technology Co., Ltd.), thioacetamide (CH_3CSNH_2, 99%, Chengdu Cologne Chemical Co., Ltd.), and nano titanium dioxide (P25, 99.9% Shanghai King Chemical Co., Ltd.), were used without any further purification.

2.2. Synthesis of 1T-MoS_2, 2H-MoS_2, and MoS_2@TiO_2. Two-dimensional (2D) composite materials of 1T-MoS_2@TiO_2 and 2H-MoS_2@TiO_2 were synthesized using the hydrothermal method. For the preparation of 1T-MoS_2@TiO_2, 96 mg of MoO_3, 112 mg of thioacetamide, and 0.96 g of urea were dissolved in 58.8 mL of deionized water and then 5.3 g of TiO_2 was added. After stirring for 2 h, the solution was transferred to a Teflon-lined autoclave reactor, which was kept in an oven at 200 °C for 12 h. Thereafter, it was cooled to room temperature and then the autoclave reactor was taken out. Finally, the as-prepared 1T-MoS_2@TiO_2 was collected and washed with deionized water and ethanol and then stored in deionized water before use. In theory, 2% 1T-MoS_2@TiO_2 was obtained based on the above statement. Composites with different compositions of MoS_2 were prepared by changing the MoO_3/urea ratio using the same procedure listed above.

2H-MoS_2@TiO_2 was synthesized using a similar method to the preparation of 1T-MoS2@TiO_2, and the only difference is that the reaction temperature was changed from 200 to 240 °C. The flow chart of the specific process is shown in Figure 1.

2.3. Photocatalytic Degradation of Tannic Acid. The photocatalytic degradation of tannic acid was carried out in a reactor (model BL-GHX-V, Shanghai Bilang Instrument Co., Ltd.). Because the light source is a 1000 W mercury lamp, which has a high heat output, the equipment is equipped with a cold trap, and water is continuously supplied to protect the equipment during the reaction. The experiment was divided into the dark response stage and the light reaction stage. The dark reaction stage was to ensure that the material and the tannic acid in the solution reach a physical adsorption−desorption equilibrium within 120 min. After the material reached the physical adsorption−desorption equilibrium, the photocatalysis reaction was carried out (m/v = 1:8 mg/mL, C_{TA} = 40 ppm, T = 300 K, UV intensity = 1000 W). During the photocatalytic reaction (dark reaction stage and light reaction stage), the tannic acid solution was sampled and

https://doi.org/10.1021/acsomega.1c02500
ACS Omega 2021, 6, 28538−28547

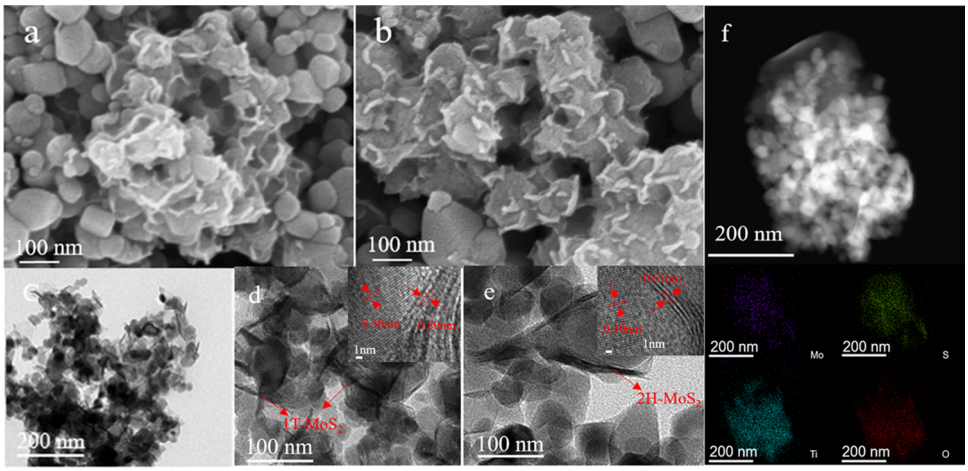

Figure 2. Microscopies of the as-synthesized samples. (a) SEM image of 16% 1T-MoS_2@TiO_2. (b) SEM image of 13% 2H-MoS_2@TiO_2. (c) TEM image of 16% 1T-MoS_2@TiO_2. (d) High-resolution TEM of 16% 1T-MoS_2@TiO_2, which shows the lattice spacing of TiO_2 and 1T-MoS_2. (e) High-resolution TEM of 13% 2H-MoS_2@TiO_2, which shows the lattice spacing of TiO_2 and 2H-MoS_2. (f) Element mapping of Mo, S, Ti, and O of 1T-MoS_2@TiO_2.

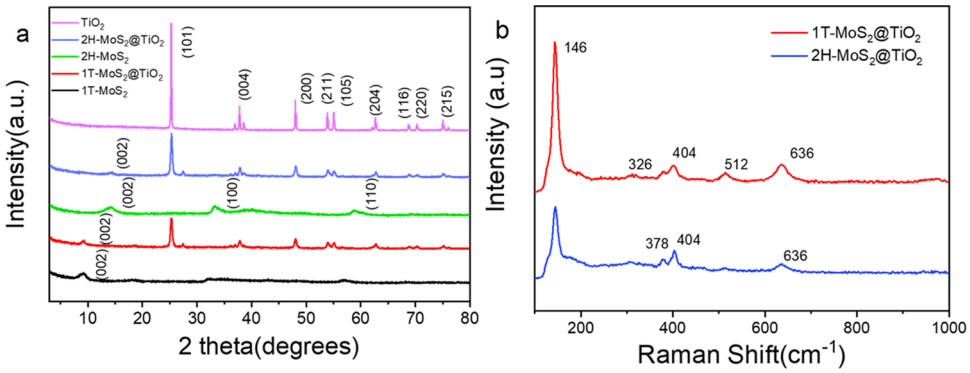

Figure 3. (a) XRD patterns of anatase TiO_2, 2H-MoS_2, 1T-MoS_2, and composite materials 1T-MoS_2@TiO_2 and 2H-MoS_2@TiO_2. (b) Raman shift of 1T-MoS_2@TiO_2 and 2H-MoS_2@TiO_2.

filtered every 20 min, and then the absorbance of tannic acid in the solution was tested with a UV2600 ultraviolet−visible spectrophotometer. Through the formula $C/C_0 = A/A_0$, the tannin concentration value was obtained.

2.4. Active Species Capture Experiment. The experiment was divided into four groups, and the amount of compound sample and tannic acid remained unchanged (m/v = 1:8, 5 mg; 40 mL, C_{TA} = 40 ppm). Isopropyl alcohol (IPA) (2 mL), ethylenediaminetetraacetic acid (EDTA) (2 mg), and Na_2SO_4 (2 mg) were added to the first three groups and the last group was a blank control. The experiment was divided into dark reaction and light reaction for 2 h each and the light source was a mercury lamp. The samples are taken for testing at the end of the dark reaction and light reaction.

2.5. Characterization. The morphology of MoS_2@TiO_2 was investigated by scanning electron microscopy (SEM, Carl Zeiss, Ultra 55) and transmission electron microscopy (TEM, Carl Zeiss, Libra 200). The elemental mapping was recorded on a TEM equipped with an energy dispersive spectrometer. Powder X-ray diffraction (XRD) patterns were performed on a Cu Kα radiation PAN analytical X-ray diffractometer. A laser Raman spectrometer (inVia) was used to analyze the samples by Raman spectroscopy. X-ray photoelectron spectroscopy (XPS, Thermo Fisher Scientific) was used to analyze the elemental composition and valence of the materials. The light absorption characteristics of the samples were carried out on a solid ultraviolet absorption spectrometer (UV−vis, Shimadzu Enterprise Management (China) Co., Ltd.) with the equipment model Solidspec-3700. UV−vis absorbance spectra were detected on a UV2600 UV−vis spectrophotometer (Unico Instruments Co., Ltd.). The Mott−Schottky curve (Mott−Schottky) and AC impedance (EIS) of the cell with the as-prepared sample as an electrolyte are examined on an electrochemical analyzer of CHI instruments (Shanghai Chenhua Instrument Company, CHI660C) and the details are shown in the Supporting information.

3. RESULTS AND DISCUSSION

3.1. Composite Materials Characterization Results. Figure 2a,b shows the scanning electron microscopy images of 1T-MoS_2@TiO_2 and 2H-MoS_2@TiO_2, respectively. It can be seen that (1T/2H) MoS_2 and TiO_2 grow together to present a sheet-like package structure, connecting into one piece and piling up. It can be seen from Figure S1a,b in the Supporting Information that 1T-MoS_2 and 2H-MoS_2 have similar particle sizes and morphology. Figure 2c,d shows the transmission microscope images of 1T-MoS_2@TiO_2. It can be seen that the gray part is TiO_2 nanoparticles, and the black banded part is 1T-MoS_2 distributed uniformly on the TiO_2 surface. The images in Figure S2a,b in the Supporting Material further

https://doi.org/10.1021/acsomega.1c02500
ACS Omega 2021, 6, 28538−28547

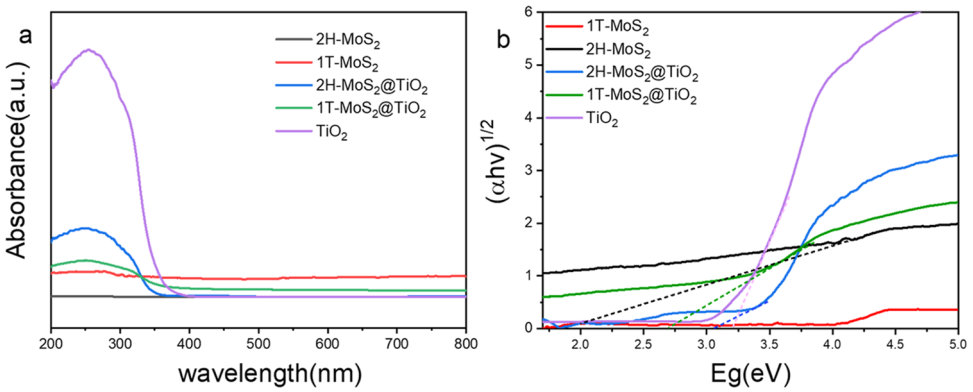

Figure 4. Optical properties of the as-prepared materials. (a) UV−vis diffuse reflectance spectra. (b) Plots of $(ah\nu)^{1/2}$ as a function of E_g photon energy.

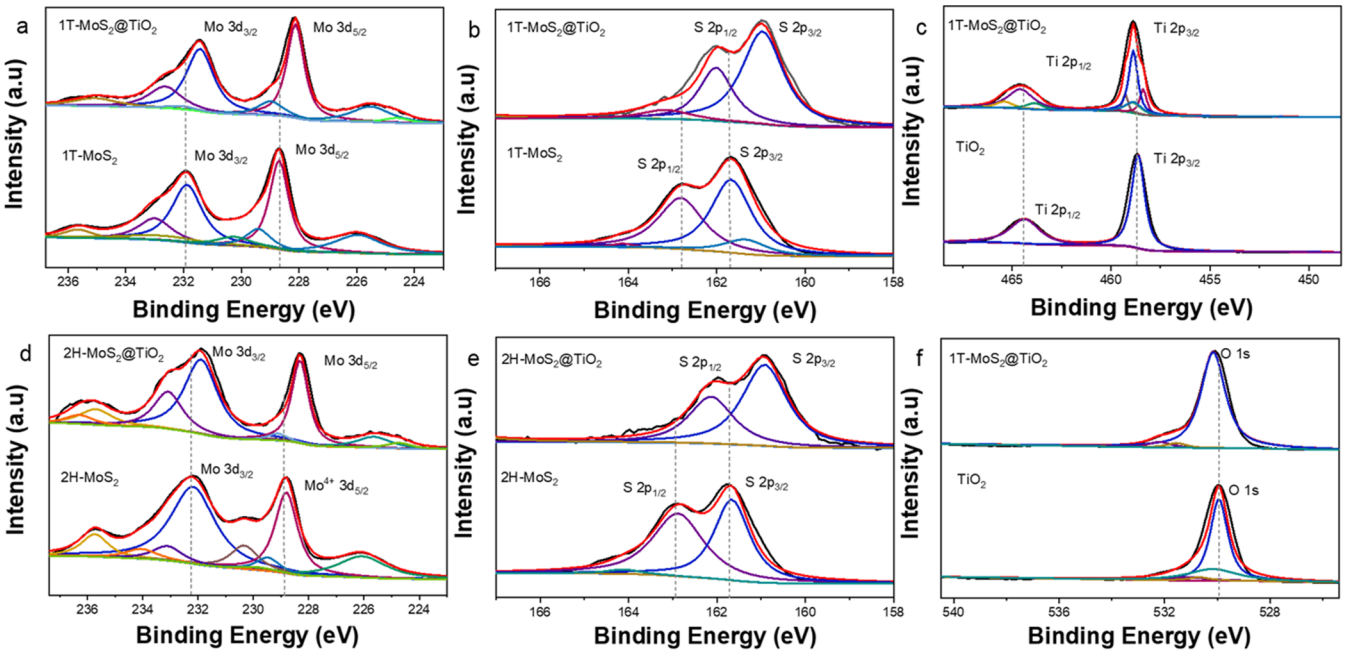

Figure 5. High-resolution XPS spectra of the as-prepared samples. (a) Mo 3d of 1T-MoS_2 and 1T-MoS_2@TiO_2. (b) S 2p of 1T-MoS_2 and 1T-MoS_2@TiO_2. (c) Ti 2p of TiO_2 and 1T-MoS_2@TiO_2. (d) Mo 3d of 2H-MoS_2 and 2H-MoS_2@TiO_2. (e) S 2p of 2H-MoS_2 and 2H-MoS_2@TiO_2. (f) O 1s of TiO_2 and 1T-MoS_2@TiO_2.

prove the uniformity of MoS_2 distributed on the TiO_2 surface. The inset in the upper right corner shows that 1T-MoS_2 has a lattice spacing of 0.89 nm corresponding to its (002) plane, and TiO_2 has a lattice spacing of 0.30 nm corresponding to its (101) plane. Figure 2e shows a high-resolution TEM image of 2H-MoS_2@TiO_2. It can be seen that the black band-like 2H-MoS_2 is also supported on the surface of TiO_2. The upper right part of Figure 2e shows that the lattice spacing of 2H-MoS_2 is 0.61 nm corresponding to its (002) plane. The lattice spacing of TiO_2 is 0.30 nm corresponding to its (101) plane. Figure 2f shows the energy-dispersive spectrometry (EDS) energy spectrum analysis of the four elements Mo, S, Ti, and O in the composite material, which indicates that MoS_2 is distributed evenly on the surface of TiO_2. The EDS results show that Mo and S are distributed in the same area. SEM and TEM analyses have proved that two components (MoS_2 and TiO_2) form a heterojunction material.

Figure 3a shows the XRD patterns of anatase TiO_2, 2H-MoS_2, 1T-MoS_2, and composite materials 1T-MoS_2@TiO_2 and 2H-MoS_2@TiO_2. The diffraction peaks of TiO_2 at 25.27, 37.77, and 47.99° correspond to (101), (004), (200) of anatase TiO_2. The peaks of 53.88, 55.05, 62.83, 68.72, 70.26, and 75.04° correspond to (211), (105), (204), (116), (220), (215) crystal planes. These results indicate that the anatase phase of TiO_2 is obtained in the current catalysts. The (002) crystal face of 2H-MoS_2 is detected at 14.37° in 2H-MoS_2@TiO_2, and the (002) crystal face unique to 1T-MoS_2 is detected at 9.12° in 1T-MoS_2@TiO_2. However, the remaining crystal planes of 2H-MoS_2 and 1T-MoS_2 are not detected, which might be due to the small proportions of these two materials in the composite samples. The XRD results indicate that the TiO_2 is distributed evenly in the composite materials. Due to the difference in the structure, their Raman characteristics are also different. Figure 3b shows the Raman spectra of the two composite materials. It can be seen that 1T-MoS_2@TiO_2 has a stronger Raman spectrum at 146 cm^{-1} than 2H-MoS_2@TiO_2, which is attributed to 1T-Mo−Mo stretching vibration in MoS_2. The Raman shift (326, 512 cm^{-1}) is related

https://doi.org/10.1021/acsomega.1c02500
ACS Omega 2021, 6, 28538−28547

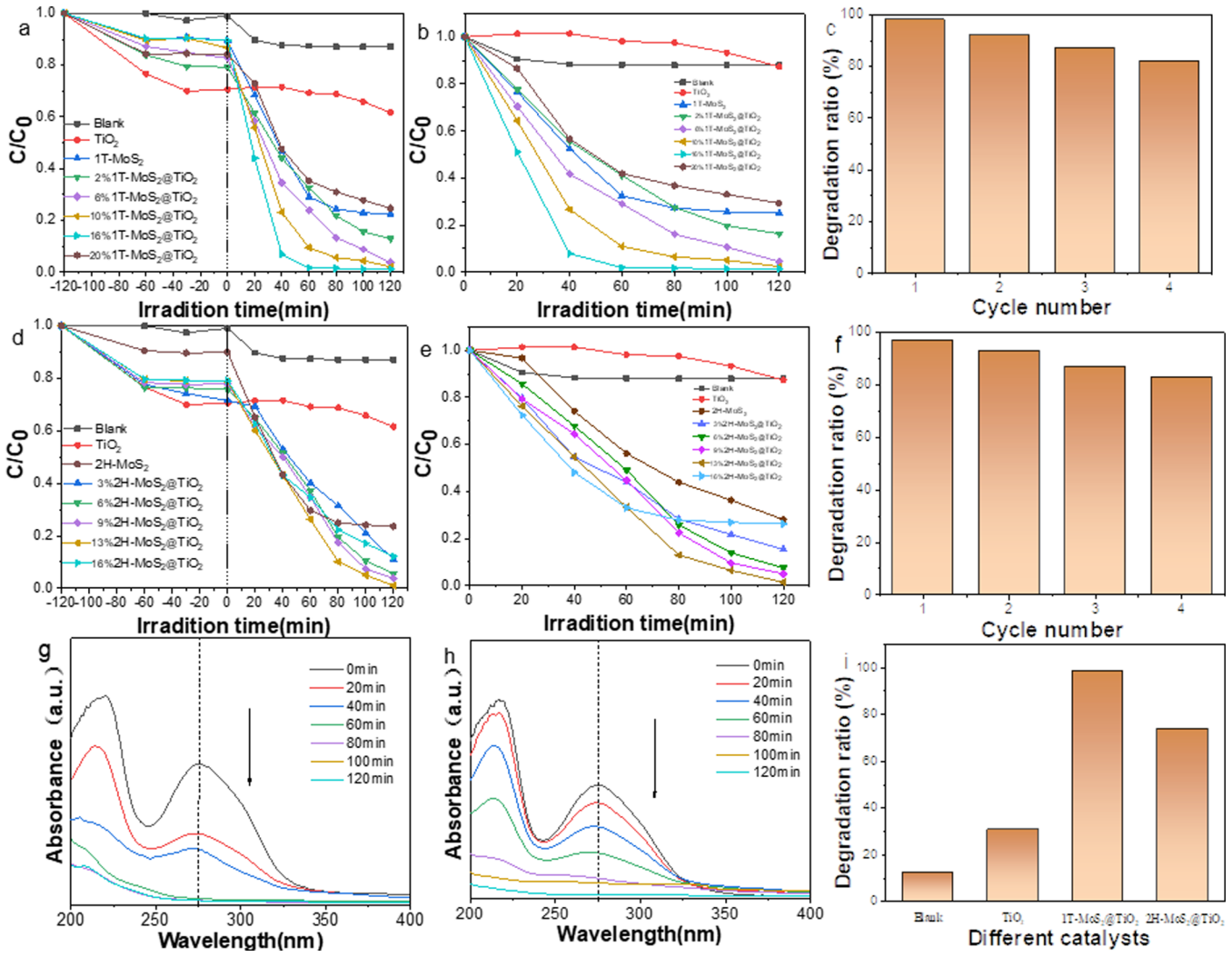

Figure 6. Photocatalytic degradation of tannic acid. (a) Photocatalytic degradation tests in the presence of the composite material loaded with different amounts of 1T-MoS_2. (b) Photocatalytic degradation stage of the composite material containing 1T-MoS_2. (c) Stability of 16% 1T-MoS_2@TiO_2. (d) Photocatalytic degradation of tannic acid in the presence of the composite material loaded with different amounts of 2H-MoS_2. (e) Photocatalytic degradation stage of the composite material containing 2H-MoS_2. (f) Stability of 13% 2H-MoS_2@TiO_2. (g) UV−vis spectrum of 16% 1T-MoS_2@TiO_2 degradation of tannic acid. (h) UV−vis spectrum of 13% 2H-MoS_2@TiO_2 degradation of tannic acid. (i) Comparison of the degradation rate with different catalysts.

to the phonon mode in 1T-MoS_2. 2H-MoS_2 exhibits typical Raman shifts of ∼378 and 404 cm^{-1} for $E_{2g}{}^1$ and A_{1g}, respectively, which are substantially different from those of 1T-MoS_2.

Figure 4 shows the UV−vis diffuse reflectance spectra of TiO_2, 2H-MoS_2, 1T-MoS_2, and their composite materials 1T-MoS_2@TiO_2 and 1T-MoS_2@TiO_2. The adsorption band below 400 nm is the intrinsic band gap of TiO_2, which is in the ultraviolet light range. 2H-MoS_2 and 1T-MoS_2 present total absorption in the tested wavelength, with an apparent absorption in the visible light range. The spectra of 1T/2H-MoS_2@TiO_2 display combined features of MoS_2 and TiO_2, having the absorption wavelength range of 200−400 nm. Figure 4b shows that the curve of $(ah\nu)^{1/2}$ changes with the photon energy. The tangent intercept is the band gap value of the material, where the band gap value of TiO_2 and 2H-MoS_2 is 3.2 and 1.9 eV, respectively. Because MoS_2 has a narrow band gap value, it can change its band gap value when combined with TiO_2. The absorption wavelength range of the two composite materials, 2H-MoS_2@TiO_2 and 1T-MoS_2@TiO_2, is between 200 and 400 nm, which is in the ultraviolet wavelength range.

XPS is used to analyze the chemical composition of the product (Figure S3 in the Supporting Material). The XPS spectra show the existence of Mo, S, Ti, and O, and the consistency of the valence state with pure MoS_2 and TiO_2. The Mo 3d spectrum of the 1T-MoS_2@TiO_2 composite material and the spectrum of pure 1T-MoS_2 are shown in Figure 5a, where the characteristic peaks of pure 1T-MoS_2 are at around 231.88 and 228.58 eV generated by Mo $3d_{3/2}$ and Mo $3d_{5/2}$ orbitals corresponding to Mo^{4+}. The Mo $3d_{3/2}$ and Mo $3d_{5/2}$ orbitals of the 1T-MoS_2@TiO_2 material have characteristic peak positions at around 231.18 and 227.98 eV, which means that the Mo^{4+} of the composite material shifts to the direction of low binding energy. Similarly, the weaker peaks produced by pure 1T-MoS_2 at 229.38 and 233.28 eV also move to the lower binding energy direction, which decreased to 229.05 and 232.72 eV, respectively. Therefore, it is proved that composite materials are more conducive to the transfer of electrons. Figure 5b shows the location of the characteristic peaks of the

https://doi.org/10.1021/acsomega.1c02500
ACS Omega 2021, 6, 28538−28547

S $2p_{1/2}$ and S $2p_{3/2}$ orbitals of pure 1T-MoS_2 at around 162.68 and 161.68 eV. The locations of the characteristic peaks of the S $2p_{1/2}$ and S $2p_{3/2}$ orbitals in the 1T-MoS_2@TiO_2 material are at around 161.98 and 160.98 eV, demonstrating that S^{2-} in the 1T-MoS_2@TiO_2 material also shifts to the low binding energy. Figure 5c,f shows the comparison spectra of Ti 2p and O 1s of 1T-MoS_2@TiO_2 and pure TiO_2, respectively. The characteristic peaks of pure TiO_2 are at around 464.38 and 458.68 eV, which correspond to Ti^{4+} by Ti $2p_{1/2}$ and Ti $2p_{3/2}$ orbitals, respectively. The position of the characteristic peaks generated by the Ti $2p_{1/2}$ and Ti $2p_{3/2}$ orbitals of 1T-MoS_2@TiO_2 is about 464.68 and 458.88 eV, the position of the characteristic peaks generated by the O 1s orbital of pure TiO_2 is about 529.98 eV, and the O 1s orbital of 1T-MoS_2@TiO_2 is at around 530.08 eV. These results show that the characteristic peaks of Ti^{4+} and O^{2-} in 1T-MoS_2@TiO_2 are shifted to the high binding energy, while the characteristic peaks of Mo^{4+} and S^{2-} are shifted to the low binding energy. This shifting demonstrates electron transfer from TiO_2 to MoS_2 and improved the successful recombination of MoS_2 and TiO_2. In Figure 5d, it can be seen that the characteristic peaks of the Mo $3d_{3/2}$ and Mo $3d_{5/2}$ orbitals of pure 2H-MoS_2 are at around 232.18 and 228.78 eV, and the Mo $3d_{3/2}$ and Mo $3d_{5/2}$ characteristic peaks of the 2H-MoS_2@TiO_2 material are located near 231.28 and 227.98 eV, so they are also shifted to the direction of low binding energy. The weaker peaks of pure 2H-MoS_2 at 229.48 and 232.98 eV also shift to the low binding energy direction, shifting to 229.35 and 232.48 eV, respectively. The shift peaks show that composite materials can accelerate electron transfer. It can be found in Figure 5e that the characteristic peaks of the S $2p_{1/2}$ and S $2p_{3/2}$ orbitals of pure 2H-MoS_2 are around 162.88 and 161.78 eV, and the characteristic peaks of the S $2p_{1/2}$ and S $2p_{3/2}$ orbitals of the 2H-MoS_2@TiO_2 material are located at the position of around 161.98 and 160.98 eV. According to the spectrum analysis, it can be seen that the comparison spectrum of Ti 2p and O 1s of 2H-MoS_2@TiO_2 and pure TiO_2 also displays the shift of the characteristic peaks of Ti^{4+} and O^{2-} of the 2H-MoS_2@TiO_2 to the direction of high binding energy (Figure S4 in the Supporting Material).

3.2. Photocatalytic Degradation of Tannic Acid. The photocatalytic activities of 1T-MoS_2@TiO_2 and 2H-MoS_2@TiO_2 were evaluated by testing the degradation rate of tannic acid (TA) in water with a concentration of 40 mg/L under ultraviolet light (a mercury lamp with a light source of 1000 W). A commercial TiO_2 was used for comparison.

Figure 6a shows the photocatalytic degradation capacity of tannic acid over blank sample, TiO_2, 1T-MoS_2, and composite materials of x% 1T-MoS_2@TiO_2 (x = 2, 6, 10, 16, 20). The data in Figure 6a shows that the composite materials are far more active than the blank, TiO_2, and 1T-MoS_2 materials with an order of x% 1T-MoS_2@TiO_2 > 1T-MoS_2 > TiO_2 > blank.

The adsorption capability of pure TiO_2 is stronger than that of the composite 1T-MoS_2@TiO_2 and 2H-MoS_2@TiO_2 materials. We can see significant desorption in the beginning of the photoreaction stage for the pure TiO_2. That is, the plot of the photodegradation of tannic acid in the first 40 min (Figure 6a,b,d,e) of the reaction has a slight increasing trend, which is due to the remarkable desorption of tannic acid adsorbed by the material in the dark reaction stage. As the photocatalytic reaction progresses, the amount of photocatalytic degradation gradually increases and then exceeds the analytical amount, so the graph shows a downward trend. Figure 6b shows the degradation plot of tannic acid regarding the typical amount of 1T-MoS_2. Significant enhancement in the degradation of 63% is achieved with 2% 1T-MoS_2 in 1 h as compared to that of 31% using the TiO_2 sample without MoS_2. A further degradation improvement is found when 1T-MoS_2 increases to 6 and 10%. The optimal amount of 1T-MoS_2 is found to be 16% with 98% degradation. The degradation efficiency is not improved by increasing the 1T-MoS_2 content to 20% or more (Figure S5).

We guess that there may be two reasons for this phenomenon. First, MoS_2 is combined with TiO_2 to form a heterojunction material, and photogenerated electrons are formed on the active sites on the surface of TiO_2 and transferred to MoS_2. Therefore, it promotes the separation of electron−hole pairs and improves the photocatalytic reaction efficiency. A negative effect was found with further increase in the MoS_2 loading. Part of the active sites on the TiO_2 surface is covered and the places where photoelectrons are generated on the TiO_2 surface reduce, resulting in a decrease in the photocatalytic degradation efficiency. Second, as the load of 1T-MoS_2 increases, the overall color of the composite material becomes darker. After adding the tannic acid solution, the whole solution becomes more turbid. During the photoreaction, part of the light source cannot reach the surface of the catalyst. Therefore, the photogenerated excitons cannot diffuse on the surface of MoS_2 and TiO_2 and form photogenerated electrons and holes. The materials cannot undergo redox reactions with tannic acid, thereby reducing the photocatalytic degradation efficiency.

Figure 6d,e shows the photocatalytic degradation of tannins using TiO_2 and the composite MoS_2@TiO_2 with different content of MoS_2. In comparison with the blank sample, TiO_2 and the composite display enhanced photocatalytic activity. In this case, we compare the degradation rate of various amounts of 2H-MoS_2 within 2 h with less activity of 2H-MoS_2@TiO_2 as compared to 1T-MoS_2@TiO_2. A distinguished enhanced photocatalytic activity was demonstrated after adding 3% 2H-MoS_2 to TiO_2. Among the content of 3, 6, 9, 13, and 16%, the best degradation of 98% is obtained on the sample of 2H-MoS_2@TiO_2 with 13% 2H-MoS_2. Figure 6c,f shows photocatalytic degradation stability experiments of tannic acid in the presence of 1T-MoS_2@TiO_2 (16%) and 2H-MoS_2@TiO_2 (13%). In the four cycles of experiments, the photocatalytic degradation efficiency gradually decreases with the number of cycles, but all exceeded 80%, indicating that the two composite materials have good stability. Figure 6g,h shows the UV−vis curves of 1T-MoS_2@TiO_2 (16%) and 2H-MoS_2@TiO_2 (13%) photocatalytic degradation of tannic acid. The peak change of tannic acid at a wavelength of 275 nm within 120 min of photoreaction was analyzed. It can be seen that the degradation rate of tannic acid in the presence of 16% 1T-MoS_2@TiO_2 reaches 98% when the photoreaction is 60 min, while 13% 2H-MoS_2@TiO_2 (13%) achieves the same degradation rate when the photoreaction is 120 min. Figure 6i compares the highest photocatalytic degradation rate of tannic acid in the presence of various materials in this study in 1 h, demonstrating that the composite material of 1T- MoS_2@TiO_2 is a highly efficient catalyst.

No matter what phase MoS_2 is, it shows excellent photocatalytic degradation performance for tannic acid. A 98% degradation rate is achieved with 16% 1T-MoS_2@TiO_2 after 60 min and the same degradation is reached with 13% 2H-MoS_2@TiO_2 after 120 min. In 120 min, the degradation

https://doi.org/10.1021/acsomega.1c02500
ACS Omega 2021, 6, 28538−28547

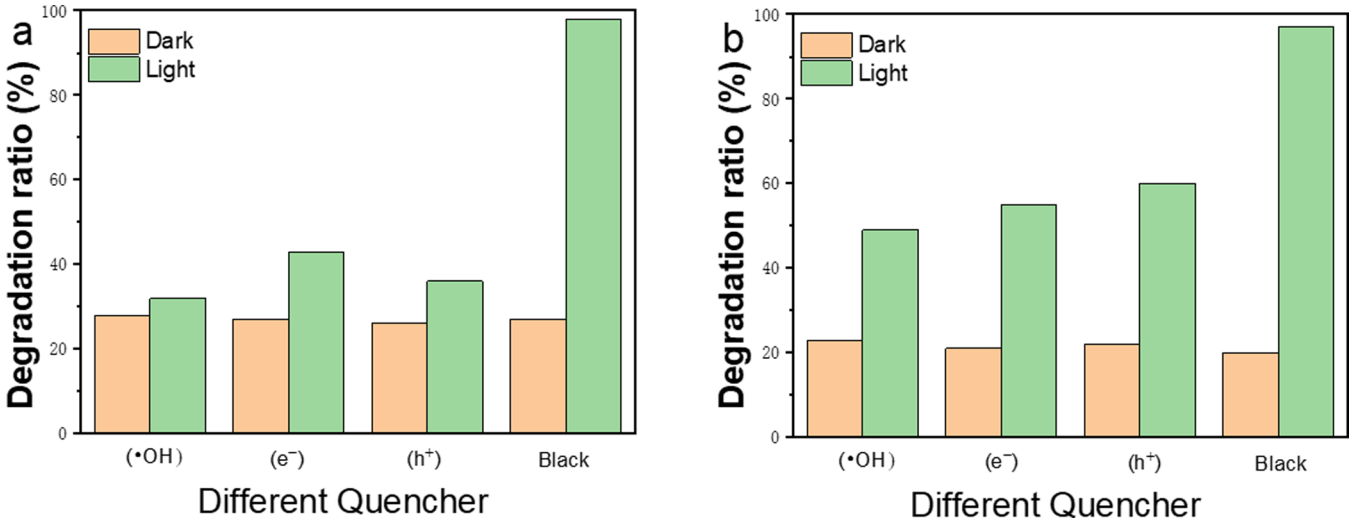

Figure 7. Degradation efficiency of the composite materials under different quenchers. (a) 1T-MoS_2@TiO_2. (b) 2H-MoS_2@TiO_2.

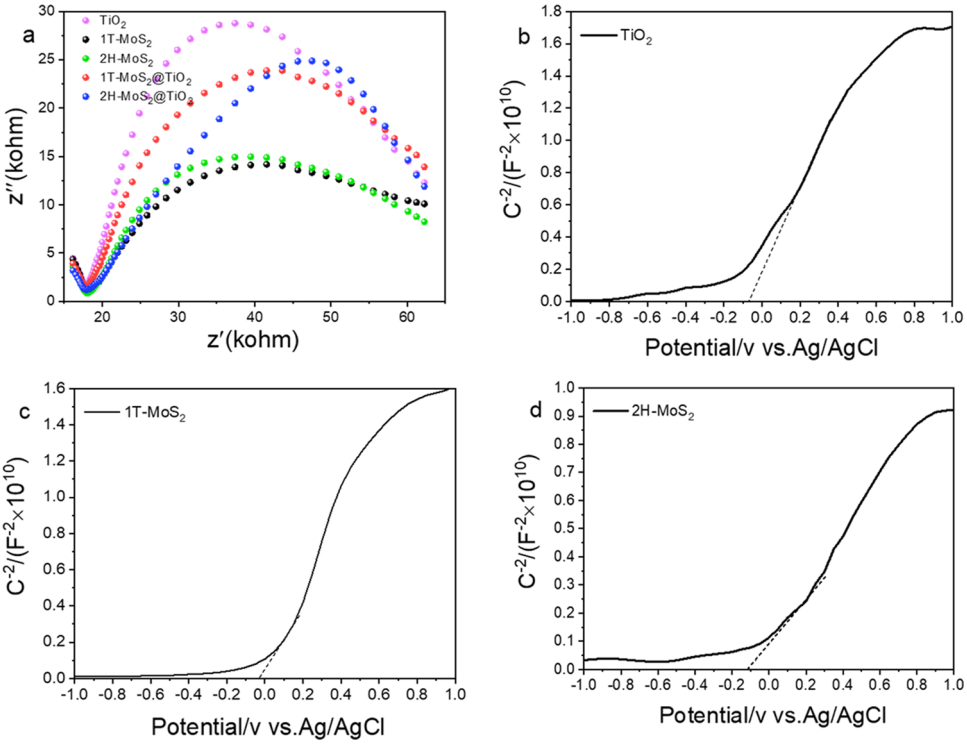

Figure 8. (a) Electrochemical impedance diagram. (b) Mott−Schottky curve of TiO_2. (c) Mott−Schottky curve of 1T-MoS_2. (d) Mott−Schottky curve of 2H-MoS_2.

rate of commercial TiO_2 is 38%. The as-prepared MoS_2@TiO_2 in this study shows much better photocatalytic activity than nano-TiO_2-coated tiles with 76% tannic acid degraded in 6 h.[53] This heterojunction material also has a comparable ability on the degradation of tannic acid using titanium oxide-coated magnetic activated carbon (m/v = 2:1, C_{TA} = 100 ppm) or Fe−N codoped SiO_2@TiO_2 (m/v = 1:1 mg/mL, C_{TA} = 30 ppm) with 98% degradation rate in 150 min and 99% degradation rate in 80 min.[52,54] It is interesting that we use less catalysts (m/v = 1:8, C_{TA} = 40 ppm) and achieve a similar performance. The significantly improved photocatalytic activity might be contributed to the large surface area, excellent electron transfer ability, and enhanced active sites of the 1T-MoS_2@TiO_2 heterojunction material. Therefore, we can see that our results are promising in terms of materials selection and degradation activity toward tannic acid.

To determine the active species involved in the degradation of tannic acid, Figure 7 shows the effect of photocatalytic degradation of tannic acid by the two composite materials after adding different quenchers. The quencher for •OH is IPA, the quencher for holes (h^+) is EDTA, and the quencher for e^- is Na_2SO_4. It can be seen from Figure 7a,b that in the dark reaction stage, the effect of the quencher on its adsorption performance is almost negligible. For the two materials in the light reaction stage, the inhibitory effect after adding IPA is significantly higher than EDTA and Na_2SO_4. That is, •OH suppression has the most significant impact on the photocatalytic performance of this material. The photogenerated

https://doi.org/10.1021/acsomega.1c02500
ACS Omega 2021, 6, 28538−28547

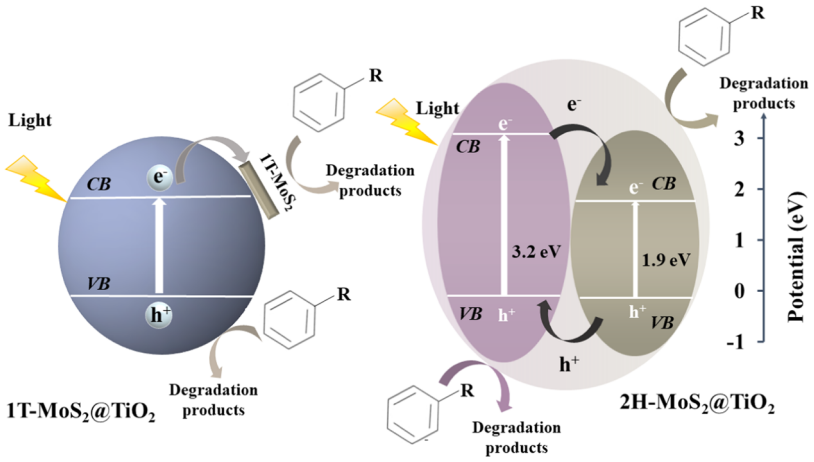

Figure 9. Schematic diagram of the photocatalytic degradation mechanism of 1T-MoS_2@TiO_2 and 2H-MoS_2@TiO_2.

electrons are absorbed by the adsorbed oxygen molecules to generate $^{\bullet}O_2^-$, the photogenerated holes generate $^{\bullet}OH$, and $^{\bullet}O_2^-$ is generated in the aqueous solution. The presence of EDTA and Na_2SO_4 hindered the formation of photogenerated $^{\bullet}O_2^-$ and holes, respectively, and affected the production of $^{\bullet}OH$ in the catalytic reaction, thereby reducing the photocatalytic performance of the composite photocatalyst.

3.3. Electrochemical Performance of MoS_2@TiO_2. The fluorine-doped tin oxide (FTO) electrode is used in photocatalytic electrochemical performance. The preparation method is shown in the Supporting Material. Figure 8a shows the electrochemical impedance of several materials. From the Nyquist diagram, it can be seen that the arc radius of 1T-MoS_2 is the smallest, the arc radius of TiO_2 is the largest, and the arc radius of 1T-MoS_2@TiO_2 is smaller than that of 2H-MoS_2@TiO_2. The high-frequency response of the Nyquist diagram is characteristic of the charge transfer process, and the arc radius of the AC impedance spectrum curve represents the resistance between the surface of the electrode material and the interface layer. The smaller the arc radius, the faster the charge transfer speed. Therefore, the surface charge transfer resistance of 1T-MoS_2@TiO_2 is less than that of 2H-MoS_2@TiO_2, which is more conducive to the separation of electrons and holes to improve the efficiency of the photocatalytic reaction. Compared with TiO_2 alone, the composite materials of 1T-MoS_2@TiO_2 and 2H-MoS_2@TiO_2 are significantly more effective in photocatalytic degradation of tannic acid. To study the conductivity and valence state of (1T/2H)-MoS_2 and TiO_2, we tested the energy band position by the Mott–Schottky (MS) method and observed from the MS curve that TiO_2 is an n-type semiconductor body. To clarify the energy band position of the material, the Mott–Schottky curves of TiO_2, 1T-MoS_2, and 2H-MoS_2 are shown in Figure 8b–d, respectively. Figure 8c shows that the 1T-MoS_2 Fermi level of the metal phase is −0.02 eV. The E_{VB} values of TiO_2 and 2H-MoS_2 are −0.07 and −0.11 V, respectively.

3.4. Photocatalytic Degradation Mechanism. Here, we try to explain the charge transfer mechanism of the two heterojunction materials. For 1T-MoS_2@TiO_2, when light is irradiated on the surface of the composite material, the MoS_2 and TiO_2 surfaces form a tight surface because 1T-MoS_2 belongs to the metal phase conductor. The large heterojunction interface can accelerate the transfer of electrons generated on the surface of TiO_2, greatly improving the efficiency of photocatalytic degradation. For 2H-MoS_2@TiO_2, when light hits the surface of the material, the photogenerated excitons diffuse rapidly on the surface of the material and dissociate into free electrons and holes at the conduction and valence bands of 2H-MoS_2 and TiO_2, respectively. The photogenerated electrons rapidly transfer from the conduction band of TiO_2 to the conduction band of MoS_2. An electron accumulation layer is formed in the conduction band of molybdenum sulfide, and a hole accumulation layer is formed in the valence band of titanium dioxide. The heterojunction enables the spatial separation of the electron–hole pairs to reduce the recombination rate effectively. The presence of MoS_2 in the two composite materials relatively shortens the original band gap value of TiO_2, enables rapid electron migration, accelerates the separation of electron and hole pairs, and improves the efficiency of the photocatalytic reaction. Figure 9 schematically depicts the two possible reaction mechanisms behind the enhanced photocatalytic performance of these materials.

4. CONCLUSIONS

In summary, the composite materials 1T-MoS_2@TiO_2 and 2H-MoS_2@TiO_2 have been successfully synthesized. The results of the photocatalytic degradation of tannic acid show that these materials have significant effects on photocatalytic activity to degrade tannic acid. Loading 16% 1T-MoS_2 and 13% 2H-MoS_2 in the composite exhibits high photocatalytic degradation capacity of 98 and 75% in 60 min, much higher than that obtained by a commercial TiO_2. The degradation speed of 16% 1T-MoS_2@TiO_2 is much higher than that of 13% 2H-MoS_2@TiO_2. We believe that the tight interface between MoS_2/TiO_2 can effectively promote the transfer of light-induced electrons and provide many active sites for photocatalytic reactions. These features are key to the high-efficiency photocatalytic activity of MoS_2@TiO_2 photocatalysts. This study demonstrates the importance of MoS_2@TiO_2, a two-dimensional material, in improving the efficiency of photocatalytic activity. It provides a new idea for photocatalytic degradation of organic acids similar to tannic acid.

■ ASSOCIATED CONTENT

Supporting Information

The Supporting Information is available free of charge at https://pubs.acs.org/doi/10.1021/acsomega.1c02500.

https://doi.org/10.1021/acsomega.1c02500
ACS Omega 2021, 6, 28538−28547

Additional FTO electrode preparation and cell configuration, SEM images and high-resolution TEM images of MoS_2@TiO_2, and XPS spectra of the as-prepared materials (PDF)

AUTHOR INFORMATION

Corresponding Authors

Cairong Jiang − *School of Materials Science and Engineering, Sichuan University of Science and Engineering, Zigong 643000, P. R. China;* orcid.org/0000-0001-8499-4062; Email: crjiang@suse.edu.cn

Tao Duan − *National Co-Innovation Center for Nuclear Waste Disposal and Environmental Safety, Southwest University of Science and Technology, Mianyang 621010, P. R. China; State Key Laboratory of Environment-friendly Energy Materials, Southwest University of Science and Technology, Mianyang 621010, P. R. China;* orcid.org/0000-0002-0944-6995; Email: duant@ustc.edu.cn

Authors

Ruixi Liu − *School of Materials Science and Engineering, Sichuan University of Science and Engineering, Zigong 643000, P. R. China; National Co-Innovation Center for Nuclear Waste Disposal and Environmental Safety, Southwest University of Science and Technology, Mianyang 621010, P. R. China; State Key Laboratory of Environment-friendly Energy Materials, Southwest University of Science and Technology, Mianyang 621010, P. R. China*

Linzhen Wu − *National Co-Innovation Center for Nuclear Waste Disposal and Environmental Safety, Southwest University of Science and Technology, Mianyang 621010, P. R. China; State Key Laboratory of Environment-friendly Energy Materials, Southwest University of Science and Technology, Mianyang 621010, P. R. China*

Hao Liu − *National Co-Innovation Center for Nuclear Waste Disposal and Environmental Safety, Southwest University of Science and Technology, Mianyang 621010, P. R. China; State Key Laboratory of Environment-friendly Energy Materials, Southwest University of Science and Technology, Mianyang 621010, P. R. China*

Youkui Zhang − *National Co-Innovation Center for Nuclear Waste Disposal and Environmental Safety, Southwest University of Science and Technology, Mianyang 621010, P. R. China; State Key Laboratory of Environment-friendly Energy Materials, Southwest University of Science and Technology, Mianyang 621010, P. R. China*

Jianjun Ma − *School of Materials Science and Engineering, Sichuan University of Science and Engineering, Zigong 643000, P. R. China;* orcid.org/0000-0002-0016-6313

Complete contact information is available at: https://pubs.acs.org/10.1021/acsomega.1c02500

Notes

The authors declare no competing financial interest.

ACKNOWLEDGMENTS

This work was funded by the National Natural Science Foundation of China (21976148), the China Basic Research Project (JCKY2018404C008), and the Sichuan Science and Technology Program (grant numbers 2019YFH0177 and 2021YFH0092).

REFERENCES

(1) Rahimi-Nasrabadi, M.; Ghaderi, A.; Banafshe, H. R.; Eghbali-Arani, M.; Akbari, M.; Ahmadi, F.; Pourmasoud, S.; Sobhani-Nasab, A. Preparation of Co2TiO4/CoTiO3/Polyaniline ternary nanohybrids for enhanced destruction of agriculture poison and organic dyes under visible-light irradiation. *J. Mater. Sci.: Mater. Electron.* **2019**, *30*, 15854−15868.

(2) Kooshki, H.; Sobhani-Nasab, A.; Eghbali-Arani, M.; Ahmadi, F.; Ameri, V.; Rahimi-Nasrabadi, M. Eco-friendly synthesis of PbTiO3 nanoparticles and PbTiO3/carbon quantum dots binary nano-hybrids for enhanced photocatalytic performance under visible light. *Sep. Purif. Technol.* **2019**, *211*, 873−881.

(3) Han, D.; Currell, M. J.; Cao, G. Deep challenges for China's war on water pollution. *Environ. Pollut.* **2016**, *218*, 1222−1233.

(4) Benitez-Navarro, J.; Salgado-Mojena, M. In *Compaction of Solid Wastes in Countries Without Disposal Facility: A Prelude of Future Troubles*, Etdeweb, 2002; pp 160−163.

(5) Rahman, R. O. A.; Ibrahium, H. A.; Hung, Y.-T. Liquid radioactive wastes treatment: a review. *Water* **2011**, *3*, 551−565.

(6) Ha, S. H.; Menchavez, R. N.; Koo, Y.-M. Reprocessing of spent nuclear waste using ionic liquids. *Korean J. Chem. Eng.* **2010**, *27*, 1360−1365.

(7) Ma, X.; Xiang, Q.; Liao, Y.; Wen, T.; Zhang, H. Visible-light-driven CdSe quantum dots/graphene/TiO2 nanosheets composite with excellent photocatalytic activity for E. coli disinfection and organic pollutant degradation. *Appl. Surf. Sci.* **2018**, *457*, 846−855.

(8) Xiang, Q.; Yu, J.; Jaroniec, M. Graphene-based semiconductor photocatalysts. *Chem. Soc. Rev.* **2012**, *41*, 782−796.

(9) Li, Q.; Li, X.; Wageh, S.; Al-Ghamdi, A.-A.; Yu, J. CdS/graphene nanocomposite photocatalysts. *Adv. Energy Mater.* **2015**, *5*, No. 1500010.

(10) Deng, D.; Novoselov, K.; Fu, Q.; Zheng, N.; Tian, Z.; Bao, X. Catalysis with two-dimensional materials and their heterostructures. *Nat. Nanotechnol.* **2016**, *11*, 218−230.

(11) Chen, B.; Bi, H.; Ma, Q.; Tan, C.; Cheng, H.; Chen, Y.; He, X.; Sun, L.; Lim, T.-T.; Huang, L. Preparation of graphene-MoS2 hybrid aerogels as multifunctional sorbents for water remediation. Science China. *Materials* **2017**, *60*, 1102−1108.

(12) Liu, X.; Ma, R.; Wang, X.; Ma, Y.; Wang, X.; et al. Graphene oxide-based materials for efficient removal of heavy metal ions from aqueous solution: A review. *Environ. Pollut.* **2019**, *252*, 62−73.

(13) Chen, B.; Meng, Y.; Sha, J.; Zhong, C.; Hu, W.; Zhao, N. Preparation of MoS2/TiO2 based nanocomposites for photocatalysis and rechargeable batteries: progress, challenges, and perspective. *Nanoscale* **2018**, *10*, 34−68.

(14) Eda, G.; Yamaguchi, H.; Voiry, D.; Fujita, T.; Chen, M.; Chhowalla, M. Photoluminescence from chemically exfoliated MoS2. *Nano Lett.* **2011**, *11*, 5111−5116.

(15) Huang, H.; Cui, Y.; Li, Q.; Dun, C.; Zhou, W.; Huang, W.; Chen, L.; Hewitt, C. A.; Carroll, D. L. Metallic 1T phase MoS2 nanosheets for high-performance thermoelectric energy harvesting. *Nano Energy* **2016**, *26*, 172−179.

(16) Voiry, D.; Salehi, M.; Silva, R.; Fujita, T.; Chen, M.; Asefa, T.; Shenoy, V. B.; Eda, G.; Chhowalla, M. Conducting MoS2 nanosheets as catalysts for hydrogen evolution reaction. *Nano Lett.* **2013**, *13*, 6222−6227.

(17) Wang, J.; Jia, H.; Guo, Y.; Zhang, Y.; Xie, Q.; Zhu, H.; Sun, J.; Shi, F.; Liu, Z.-H.; Jiang, R. (TiO2 (B) Nanosheet)/(Metallic Phase MoS2) Hybrid Nanostructures: An Efficient Catalyst for Photocatalytic Hydrogen Evolution. *Solar RRL* **2019**, *3*, No. 1900323.

(18) Shi, S.; Sun, Z.; Hu, Y. H. Synthesis, stabilization and applications of 2-dimensional 1T metallic MoS2. *J. Mater. Chem. A.* **2018**, *6*, 23932−23977.

(19) Zhang, L.; Wu, L.; Feng, Z.; Meng, Q.; Li, Y.; Duan, T. Adopting sulfur-atom sharing strategy to construct CoS2/MoS2 heterostructure on three-dimensional nitrogen-doped graphene aerogels: A novel photocatalyst for wastewater treatment. *J. Environ. Chem. Eng.* **2020**, *9*, No. 104771.

(20) Schneider, J.; Matsuoka, M.; Takeuchi, M.; Zhang, J.; Horiuchi, Y.; Anpo, M.; Bahnemann, D. W. Understanding TiO2 photocatalysis: mechanisms and materials. *Chem. Rev.* **2014**, *114*, 9919−9986.
(21) Asahi, R.; Morikawa, T.; Irie, H.; Ohwaki, T. Nitrogen-doped titanium dioxide as visible-light-sensitive photocatalyst: designs, developments, and prospects. *Chem. Rev.* **2014**, *114*, 9824−9852.
(22) Liang, Y.; Wang, H.; Casalongue, H. S.; Chen, Z.; Dai, H. TiO2 nanocrystals grown on graphene as advanced photocatalytic hybrid materials. *Nano Res.* **2010**, *3*, 701−705.
(23) Tang, X.; Chu, W.; Qian, J.; Lin, J.; Cao, G. Low Temperature Synthesis of Large-Size Anatase TiO2 Nanosheets with Enhanced Photocatalytic Activities. *Small* **2017**, *13*, No. 1701964.
(24) Sun, C.; Xu, Q.; Xie, Y.; Ling, Y.; Hou, Y. Designed synthesis of anatase−TiO2(B) biphase nanowire/ZnO nanoparticle heterojunction for enhanced photocatalysis. *J. Mater. Chem. A* **2018**, *6*, 8289−8298.
(25) Setvin, M.; Shi, X.; Hulva, J.; Simschitz, T.; Parkinson, G. S.; Schmid, M.; Di Valentin, C.; Selloni, A.; Diebold, U. Methanol on Anatase TiO2(101): Mechanistic Insights into Photocatalysis. *ACS Catal.* **2017**, *7*, 7081−7091.
(26) Wu, L.; Fu, C.; Huang, W. Surface chemistry of TiO2 connecting thermal catalysis and photocatalysis. *Phys. Chem. Chem. Phys.* **2020**, *22*, 9875−9909.
(27) Li, G.; Ciston, S.; Saponjic, Z. V.; Chen, L.; Dimitrijevic, N. M.; Rajh, T.; Gray, K. A. Synthesizing mixed-phase TiO2 nanocomposites using a hydrothermal method for photo-oxidation and photoreduction applications. *J. Catal.* **2008**, *253*, 105−110.
(28) Nekooie, R.; Shamspur, T.; Mostafavi, A. Novel CuO/TiO2/PANI nanocomposite: Preparation and photocatalytic investigation for chlorpyrifos degradation in water under visible light irradiation. *J. Photochem. Photobiol., A* **2021**, *407*, No. 113038.
(29) Liu, X.; Wang, Y.; Zhang, T. C.; Xiang, G.; Wang, X.; Yuan, S. One-Pot Synthesis of a Magnetic TiO2/PTh/γ-Fe2O3 Heterojunction Nanocomposite for Removing Trace Arsenite via Simultaneous Photocatalytic Oxidation and Adsorption. *Ind. Eng. Chem. Res.* **2021**, *60*, 528−540.
(30) Wang, D.; Kanhere, P.; Li, M.; Tay, Q.; Tang, Y.; Huang, Y.; Sum, T. C.; Mathews, N.; Sritharan, T.; Chen, Z. Improving photocatalytic H2 evolution of TiO2 via formation of {001}−{010} quasi-heterojunctions. *J. Phys. Chem. C* **2013**, *117*, 22894−22902.
(31) Banerjee, B.; Amoli, V.; Maurya, A.; Sinha, A. K.; Bhaumik, A. Green synthesis of Pt-doped TiO2 nanocrystals with exposed (001) facets and mesoscopic void space for photo-splitting of water under solar irradiation. *Nanoscale* **2015**, *7*, 10504−10512.
(32) Xing, M.-Y.; Yang, B.-X.; Yu, H.; Tian, B.-Z.; Bagwasi, S.; Zhang, J.-L.; Gong, X.-Q. Enhanced photocatalysis by Au nanoparticle loading on TiO2 single-crystal (001) and (110) facets. *J. Phys. Chem. Lett.* **2013**, *4*, 3910−3917.
(33) Han, X.; Kuang, Q.; Jin, M.; Xie, Z.; Zheng, L. Synthesis of titania nanosheets with a high percentage of exposed (001) facets and related photocatalytic properties. *J. Am. Chem. Soc.* **2009**, *131*, 3152−3153.
(34) Tang, Q.; Jiang, D.-e. Mechanism of Hydrogen Evolution Reaction on 1T-MoS2 from First Principles. *ACS Catal.* **2016**, *6*, 4953−4961.
(35) Kibombo, H. S.; Peng, R.; Rasalingam, S.; Koodali, R. T. Versatility of heterogeneous photocatalysis: synthetic methodologies epitomizing the role of silica support in TiO2 based mixed oxides. *Catal. Sci. Technol.* **2012**, *2*, 1737−1766.
(36) Tang, J.; Cowan, A. J.; Durrant, J. R.; Klug, D. R. Mechanism of O2 production from water splitting: nature of charge carriers in nitrogen doped nanocrystalline TiO2 films and factors limiting O2 production. *J. Phys. Chem. C.* **2011**, *115*, 3143−3150.
(37) Khan, G.; Kim, Y. K.; Choi, S. K.; Han, D. S.; Abdel-Wahab, A.; Park, H. Evaluating the catalytic effects of carbon materials on the photocatalytic reduction and oxidation reactions of TiO2. *Bull. Korean Chem. Soc.* **2013**, *34*, 1137−1144.
(38) Seshadri, H.; Kumar, K.; Garg, M.; Velavendan, P.; Ganesh, S.; Sinha, P. Synthesis, characterization and evaluation of nanocrystalline anatase titania for the degradation of dibutyl phosphate. *J. Radioanal. Nucl. Chem.* **2014**, *300*, 157−162.
(39) Guo, H.; Kemell, M.; Heikkilä, M.; Leskelä, M. Noble metal-modified TiO2 thin film photocatalyst on porous steel fiber support. *Appl. Catal., B* **2010**, *95*, 358−364.
(40) Crake, A.; Christoforidis, K. C.; Kafizas, A.; Zafeiratos, S.; Petit, C. CO2 capture and photocatalytic reduction using bifunctional TiO2/MOF nanocomposites under UV−vis irradiation. *Appl. Catal., B* **2017**, *210*, 131−140.
(41) Harris, J.; Silk, R.; Smith, M.; Dong, Y.; Chen, W.-T.; Waterhouse, G. I. Hierarchical TiO2 nanoflower photocatalysts with remarkable activity for aqueous methylene blue photo-oxidation. *ACS Omega* **2020**, *5*, 18919−18934.
(42) Wei, X.; Xie, T.; Peng, L.; Fu, W.; Chen, J.; Gao, Q.; Hong, G.; Wang, D. Effect of heterojunction on the behavior of photogenerated charges in Fe3O4@Fe2O3 nanoparticle photocatalysts. *J. Phys. Chem. C* **2011**, *115*, 8637−8642.
(43) Cheng, L.; Zhang, D.; Liao, Y.; Li, F.; Zhang, H.; Xiang, Q. Constructing functionalized plasmonic gold/titanium dioxide nanosheets with small gold nanoparticles for efficient photocatalytic hydrogen evolution. *J. Colloid Interface Sci.* **2019**, *555*, 94−103.
(44) Chhowalla, M.; Shin, H. S.; Eda, G.; Li, L.-J.; Loh, K. P.; Zhang, H. The chemistry of two-dimensional layered transition metal dichalcogenide nanosheets. *Nat. Chem.* **2013**, *5*, 263−275.
(45) Zeng, Z.; Yin, Z.; Huang, X.; Li, H.; He, Q.; Lu, G.; Boey, F.; Zhang, H. Single-Layer Semiconducting Nanosheets: High-yield preparation and device fabrication. *Angew. Chem.* **2011**, *123*, 11289−11293.
(46) Kuru, C. Controlled Vanadium Doping of MoS2 Thin Films Through Co-sputtering and Thermal Sulfurization. *Cumhuriyet Sci. J.* **2020**, *41*, 305−310.
(47) Kibsgaard, J.; Chen, Z.; Reinecke, B. N.; Jaramillo, T. F. Engineering the surface structure of MoS2 to preferentially expose active edge sites for electrocatalysis. *Nat. Mater.* **2012**, *11*, 963−969.
(48) Chang, K.; Mei, Z.; Wang, T.; Kang, Q.; Ouyang, S.; Ye, J. MoS2/graphene cocatalyst for efficient photocatalytic H2 evolution under visible light irradiation. *ACS nano.* **2014**, *8*, 7078−7087.
(49) Lukowski, M. A.; Daniel, A. S.; Meng, F.; Forticaux, A.; Li, L.; Jin, S. Enhanced hydrogen evolution catalysis from chemically exfoliated metallic MoS2 nanosheets. *J. Am. Chem. Soc.* **2013**, *135*, 10274−10277.
(50) Yuan, Y.-J.; Ye, Z.-J.; Lu, H.-W.; Hu, B.; Li, Y.-H.; Chen, D.-Q.; Zhong, J.-S.; Yu, Z.-T.; Zou, Z.-G. Constructing Anatase TiO2 Nanosheets with Exposed (001) Facets/Layered MoS2 Two-Dimensional Nanojunctions for Enhanced Solar Hydrogen Generation. *ACS Catal.* **2016**, *6*, 532−541.
(51) Tang, Y.; Yin, X.; Mu, M.; Jiang, Y.; Li, X.; Zhang, H.; Ouyang, T. Anatase TiO2@MIL-101(Cr) nanocomposite for photocatalytic degradation of bisphenol A. *Colloids Surf., A* **2020**, No. 124745.
(52) Li, Y.; Zhai, Y.; Zhang, P.; Wang, X.; Cui, H.; Li, J.; Liu, L.; Zhao, H.; Song, J. Synthesis of titania coated magnetic activated carbon for effective photodegradation of tannic acid in aqueous solution. *Colloids Surf., A* **2019**, *563*, 141−147.
(53) Qiu, Z.; Yang, Q.; Liu, W. Photocatalytic degradation of phytotoxic substances in waste nutrient solution by various immobilized levels of nano-TiO2. *Water, Air, Soil Pollut.* **2013**, *224*, No. 1461.
(54) Wan, H.; Yao, W.; Zhu, W.; Tang, Y.; Ge, H.; Shi, X.; Duan, T. Fe-N co-doped SiO2@TiO2 yolk-shell hollow nanospheres with enhanced visible light photocatalytic degradation. *Appl. Surf. Sci.* **2018**, *444*, 355−363.
(55) Geng, X.; Sun, W.; Wu, W.; Chen, B.; Al-Hilo, A.; Benamara, M.; Zhu, H.; Watanabe, F.; Cui, J.; Chen, T.-p. Pure and stable metallic phase molybdenum disulfide nanosheets for hydrogen evolution reaction. *Nat. Commun.* **2016**, *7*, No. 10672.

https://doi.org/10.1021/acsomega.1c02500
ACS Omega 2021, 6, 28538−28547